

# Nanoarchitectonics of Biofunctionalized Hydrogen-Terminated 2D-Germanane Heterostructures as Highly Sensitive Biorecognition Transducers: The Case Study of Cocaine Drug

Yiming Lei, Ángel Campos-Lendínez, Xavier Sala, Jordi García-Antón,\*  
and Jose Muñoz\*

Hydrogen-terminated 2D-germanane (2D-GeH), as one inorganic 2D material akin to graphene, is attracting widespread interest owing to its predicted (opto) electronic properties. Nonetheless, the chemical reactivity of 2D-GeH requires further exploration to expand its real implementation. Herein, a simple and straightforward bottom-up biofunctionalization approach is reported aiming at providing the bases toward the robust design of 2D-GeH-based biorecognition systems with electrical readout. For this goal, 2D-GeH has been firstly functionalized with gold nanoparticles (Au-NPs) via an organometallic approach, followed by the covalent immobilization of a thiolated single-stranded DNA (ssDNA) aptamer via Au–S bond interactions. After an accurate material characterization, the resulting ssDNA/Au@GeH heterostructure is drop-casted on a fluorine-doped tin oxide (FTO) electrode for impedimetrically monitoring cocaine as a model drug. Interestingly, the aptamer–cocaine interactions hinder the interfacial electron-transfer process of the benchmark  $[\text{Fe}(\text{CN})_6]^{3-/4-}$  redox marker with increasing concentration of the cocaine target, leading to a detection limit as low as  $4.9 \pm 0.1$  aM, the lowest one reported in literature by far. Overall, the ssDNA/Au@GeH electrochemical biosensor exhibits outstanding selectivity, specificity, and reproducibility, demonstrating the potential use of 2D-GeH as an emerging highly sensitive transducer for biosensing applications. The reported method is general and might be simply customized by tailoring the biorecognition component.


## 1. Introduction

Two-dimensional (2D) materials, as atomically thin layer materials, allow free movement of electrons in the 2D plane, making them excellent substrates to lead the next “nanoelectronics revolution”.<sup>[1–6]</sup> Having demonstrated the successful real-life implementation of graphene in very distinctive applications,<sup>[7–10]</sup> its zero bandgap has moved the materials science community to explore alternative Group-IV monoelemental 2D materials made of honeycomb-like  $sp^3$ -hybridized network layer structures, coined as Xenes (viz. silicene, germanene, stanine, and plumbene).<sup>[11,12]</sup> In particular, 2D germanene (2D-Ge) and its corresponding ligand-terminated derivatives have demonstrated unique properties, such as high electrical conductivity, semiconducting properties, and large surface area plenty of active sites that might favour (bio)functionalization,<sup>[13–16]</sup> features that foresee their potential use in the field of electrochemical biosensors. In this regard, germanium, together with silicon, are the base materials for modern electronic devices (i.e., electrochemical systems).<sup>[17]</sup>

Nonetheless, considering that 2D-Ge derivatives are emerging inorganic 2D materials, most of the research in this field has been devoted to either theoretical works<sup>[18,19]</sup> or experimental works employing weak physisorption (bio)functionalization approaches.<sup>[20–22]</sup> Among the wide library of ligand-terminated 2D-Ge, hydrogen-terminated 2D-GeH is a very interesting material owing to its simple synthetic protocol based on the topochemical deintercalation of a layered Zintl phase ( $\text{CaGe}_2$ ) in acidic media,<sup>[13]</sup> resulting in the lonely available Xene in the market.

Herein, motivated by the desire to elucidate the suitability of 2D-GeH as an unconventional transducing system to harbour biorecognition components, a general and straightforward biofunctionalization strategy has been devised for the robust design of electrochemical biosensors. The bottom-up biofunctionalization architecture relies on two-sequential steps: i) decoration of 2D-GeH with gold nanoparticles (Au-NPs) via organometallic

Y. Lei, Á. Campos-Lendínez, X. Sala, J. García-Antón, J. Muñoz  
Departament de Química  
Universitat Autònoma de Barcelona  
08193 Cerdanyola del Vallès, Barcelona, Spain  
E-mail: Jordi.GarciaAnton@uab.es; JoseMaria.Munoz@uab.cat

 The ORCID identification number(s) for the author(s) of this article can be found under <https://doi.org/10.1002/ssstr.202400240>.

© 2024 The Author(s). Small Structures published by Wiley-VCH GmbH. This is an open access article under the terms of the Creative Commons Attribution License, which permits use, distribution and reproduction in any medium, provided the original work is properly cited.

DOI: 10.1002/ssstr.202400240

(OM) approach,<sup>[23]</sup> using them not only as electrochemical signal amplifiers, but also as nanotemplates for ii) covalently anchoring thiolated biorecognition components via Au–S bond formation. As a proof-of-principle, the electrochemical determination of cocaine was interrogated as a model target, while a thiolated single-stranded DNA (ssDNA) aptamer was employed as a specific biorecognition unit to bind cocaine; see **Scheme 1** for illustration. Briefly, cocaine is an important addictive stimulant drug isolated from coca plant leaves that can promote instantaneous and adverse effects on human health, being necessary its determination for both law enforcement and clinical diagnosis.<sup>[24,25]</sup> Indeed, the cocaine-binding aptamer approach has been commonly utilized for developing different optical and electrochemical biosensing systems.<sup>[26,27]</sup> In this work, the electroanalytical assay is focused on drop-casting the resulting ssDNA/Au@GeH heterostructure on a fluorine-doped tin oxide (FTO) electrode for impedimetrically monitoring the specific aptamer–cocaine binding by means of charge transfer resistance ( $R_{CT}$ ) under the presence of a benchmark redox marker (i.e.,  $[\text{Fe}(\text{CN})_6]^{3-/4-}$ ). In this regard, electrochemical impedance spectroscopy (EIS) is known to be a powerful tool to monitor small changes in the interfacial properties of electrode surfaces.<sup>[28]</sup> Remarkably, the synergism of combining large surface area 2D materials like 2D-GeH—rich in biorecognition units via surface engineering—with impedimetric readouts resulted in a ssDNA/Au@GeH electrochemical biosensor with selective ability to determine cocaine at the attomolar (aM) level, the lowest detection limit found in literature so far. Accordingly, this work provides a general covalent biofunctionalization strategy for the development of a new family of highly sensitive electrochemical biosensors made of commercially available 2D-GeH, which

might further endow for the selective determination of alternative targets by simply tailoring the thiolated biorecognition component.

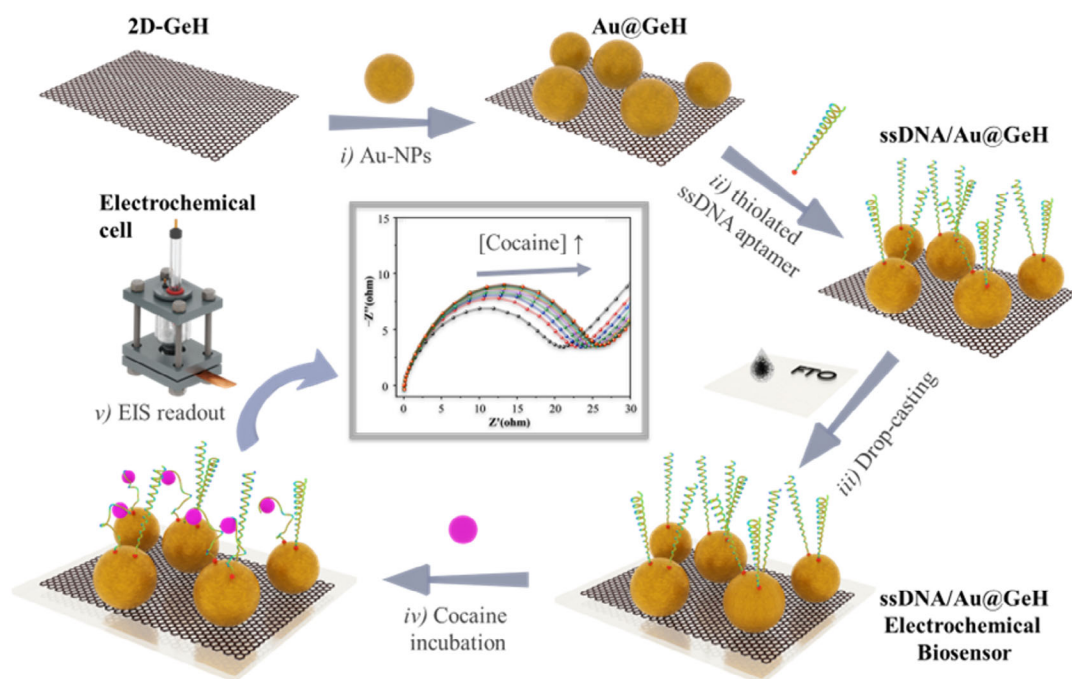
## 2. Results and Discussion

### 2.1. Synthesis and Structural Characterization of ssDNA/Au@GeH Heterostructures

The surface engineering related to the fabrication of the ssDNA/Au@GeH heterostructure implies the functionalization of pristine 2D-GeH following two consecutive stages, as illustrated in Scheme 1: i) Firstly, pristine 2D-GeH was functionalized with Au-NPs using the OM approach.<sup>[29]</sup> To do this, 10 mg of 2D-GeH were mixed in a Fisher-Porter bottle with 0.16 mg of  $[\text{Au}(\text{tht})\text{Cl}]$  (Au/GeH 1% w/w) using 10 mL of degassed THF as the solvent. Then, the mixture was pressurized under 3 bars of  $\text{H}_2$  and stirred overnight, resulting in the Au@GeH heterostructure. ii) Secondly, the Au-NPs were used as nanotemplates for covalently immobilizing the thiolated ssDNA aptamer via Au–S bond interactions. Thus, the Au@GeH heterostructure was mixed with a 16.8 nmol ssDNA aptamer solution for 12 h under stirring conditions.

The characterization of the prepared ssDNA/Au@GeH heterostructure was conducted by means of transmission electron microscopy (TEM), UV-Vis spectroscopy, Fourier-transform infrared spectroscopy (FTIR), and X-ray photoelectron spectroscopy (XPS).

Firstly, the morphology of the pristine 2D-GeH, the intermediate Au@GeH, and the final ssDNA/Au@GeH heterostructure was determined by TEM. **Figure 1a** shows the typical platelet-like



**Scheme 1.** Synthesis and fabrication of the ssDNA/Au@GeH electrochemical biosensor. Schematic illustration of the biofunctionalization approach for the fabrication of the ssDNA/Au@GeH heterostructure, and their subsequent integration on a FTO electrode for the EIS determination of the cocaine drug in a three-electrode configuration cell via cocaine-binding ssDNA aptamer.

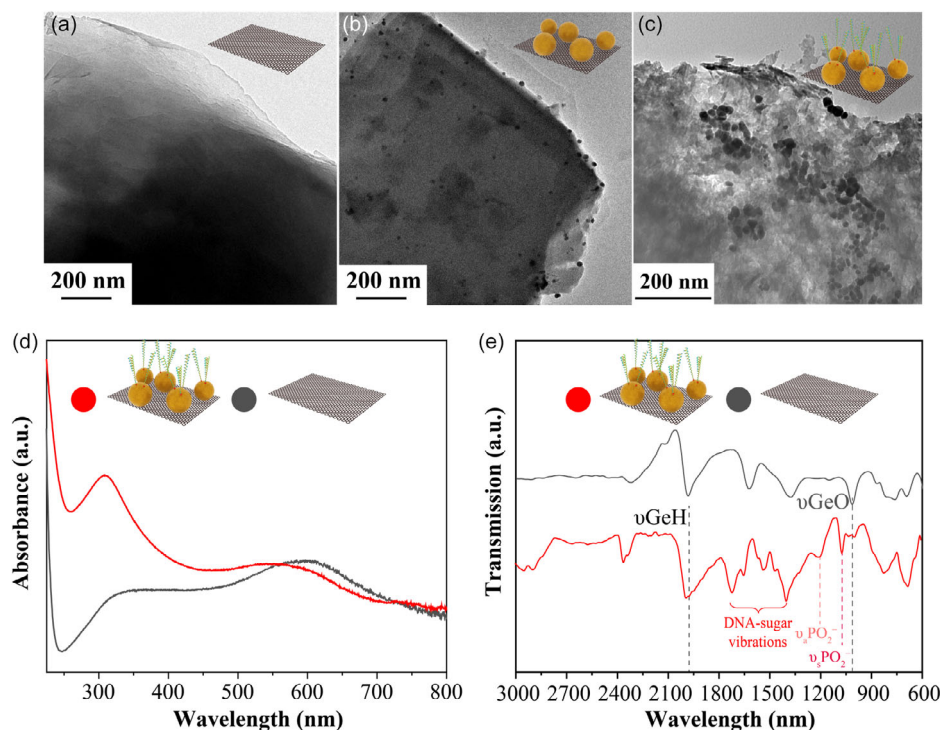


**Figure 1.** Material characterization of the ssDNA/Au@GeH heterostructure. TEM images of a) pristine 2D-GeH, b) Au@GeH, and c) ssDNA/Au@GeH. d) UV-Vis and e) FTIR spectra of pristine 2D-GeH and ssDNA/Au@GeH heterostructure.

aspect of pristine 2D-GeH with several lateral sizes formed of various stacked smooth layers.<sup>[30]</sup> After the immobilization of Au-NPs via the OM approach, the Au@GeH heterostructure clearly displayed spherical and homogeneously distributed nanoparticles with an average size of  $19.0 \pm 6.7$  nm (Figure 1b), suggesting the successful decoration of the 2D-Xene. Then, the morphological aspect of the resulting ssDNA/Au@GeH heterostructure displayed uneven walls due to the organic nature of the biorecognition unit (Figure 1c). In addition, the elemental analysis of the samples was carried out by means of energy-dispersive X-ray (EDX) spectroscopy (see Figure S1, Supporting Information). The EDX spectra of the ssDNA/Au@GeH heterostructure confirmed the coexistence of Au, S, and P with the Ge sheets. This can be seen as the first evidence of the proper immobilization of both Au-NPs and thiolated biorecognition units. Next, the optical properties of the ssDNA/Au@GeH heterostructure were evaluated by UV-Vis spectroscopy (Figure 1d). The UV-Vis spectrum of the pristine 2D-GeH shows a strong absorption in the visible spectral region, with a maximum band centered at 603 nm, according to the literature.<sup>[31]</sup> After biofunctionalization, this band was widened and blue shifted with a maximum absorption wavelength at 530 nm, which might be attributed to the plasmon contribution of Au-NPs.<sup>[32]</sup> Remarkably, an additional band centered at 307 nm was observed, indicating the presence of the ssDNA aptamer.<sup>[33]</sup>

FTIR measurements were also run to provide the first evidence of the proper biofunctionalization of the 2D-Xene. FTIR spectra of 2D-GeH before and after biofunctionalization are presented in Figure 1e. Pristine 2D-GeH exhibited a main band

centered at  $1987\text{ cm}^{-1}$  associated with  $\nu\text{GeH}$  stretching mode,<sup>[34]</sup> while the band at  $1016\text{ cm}^{-1}$  can be ascribed to  $\nu\text{GeO}$  stretching mode from the spontaneous oxidation of the 2D-GeH in air. In contrast, the presence of ssDNA aptamer was confirmed by means of DNA-sugar vibration in the range of  $1753\text{--}1472\text{ cm}^{-1}$ , which can be attributed to guanine, thymine, adenine, and cytosine nucleotides from higher to lower wavenumbers.<sup>[35]</sup> Further, the ssDNA/Au@GeH heterostructure also revealed the asymmetric ( $\nu_{\text{as}}\text{PO}_2^-$ ) and symmetric ( $\nu_{\text{s}}\text{PO}_2^-$ ) vibrations of phosphate groups from the nucleic acids centered at 1196 and  $1064\text{ cm}^{-1}$ , respectively, while the  $\nu\text{GeO}$  stretching mode almost disappeared, suggesting that the biofunctionalization method might prevent the oxidation of the 2D material. This behavior can be ascribed to the anchoring of the organic layer (viz. ssDNA aptamer), which might help to maintain the original form of 2D-GeH against air oxidation. Indeed, organic layers have already been shown to passivate 2D materials.<sup>[36,37]</sup>

Finally, the surface chemical composition of pristine 2D-GeH and ssDNA/Au@GeH heterostructure was addressed by means of XPS, as shown in Figure 2. The XPS analysis of Au@GeH (control sample) was also acquired for comparison (see Figure S2, Supporting Information). In line with the literature,<sup>[14]</sup> the deconvolution of the signal recorded for electrons excited from Ge  $3d$  orbitals of pristine 2D-GeH gave rise to three components located at ca. 29.0, 30.2, and 31.6 eV, corresponding to the Ge—Ge, Ge—H, and Ge—O, respectively (Figure 2a). After functionalization with Au-NPs, the resulting Au@GeH exhibited the same three contributions in the high-resolution Ge  $3d$  core spectrum since each direct chemical bond was formed on the

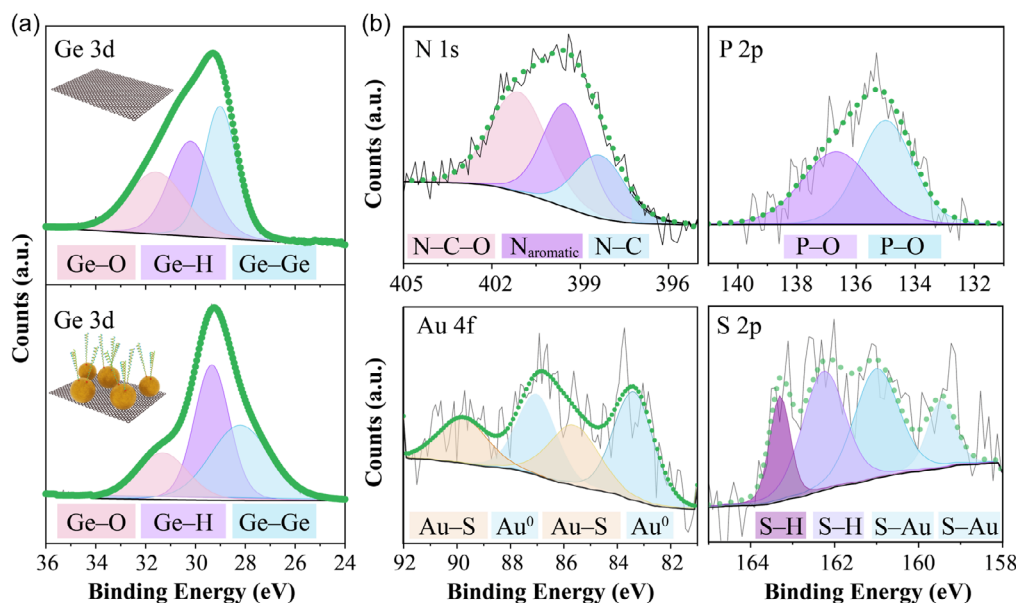


**Figure 2.** Chemical composition of ssDNA/Au@GeH heterostructure. a) High-resolution XPS spectra of Ge 3d for pristine 2D-GeH (top) and ssDNA/Au@GeH (bottom). b) High-resolution XPS spectra of Au 4f, S 2p, N 1s, and P 2p for ssDNA/Au@GeH.

2D-GeH surface. However, the Ge—Ge and Ge—H components were shifted to higher binding energies (see Table S1, Supporting Information for further details), which must be explained by the higher electronegativity of the Au atoms from the immobilized Au-NPs (Figure S2a, Supporting Information).<sup>[38]</sup> Then, the bio-functionalization with ssDNA aptamer led to a reverse shift in the Ge 3d spectrum, evidencing a change in the surrounding environment of the 2D-Xene due to the anchoring.

Further, the successful synthesis of the ssDNA/Au@GeH heterostructure was verified by the deconvolution of the signal associated with excited electrons from Au 4f, S 2p, N 1s, and P 2p (Figure 2b). Firstly, the high-resolution Au 4f core level spectrum of ssDNA/Au@GeH was mainly composed of the 4f<sub>7/2</sub> and 4f<sub>5/2</sub> components peaked at 83.4 and 87.0 eV, respectively, indicating that Au-NPs exist in their metallic form (Au<sup>0</sup>). Comparing to the Au 4f core level spectrum of Au@GeH (Figure S2b, Supporting Information), an additional doublet contribution located at 85.6 and 89.8 eV was clearly observed after grafting the ssDNA aptamer, which must be attributed to the Au—S bond contribution.<sup>[39]</sup> Remarkably, the Au 4f peaks were slightly shifted toward the lower-binding-energy region when compared to the standard values of the bulk Au metal (see Table S1, Supporting Information),<sup>[40]</sup> pointing out the strong interaction between Au and the 2D-Xene support.<sup>[41]</sup> Then, the covalent anchoring of the thiolated biorecognition component (i.e., ssDNA aptamer) via Au—S interactions was also confirmed by the signals found in the high-resolution XPS spectra of S 2p, in which two doublets (2p<sub>3/2</sub> and 2p<sub>1/2</sub>) were assigned to the thiolate Au—S bounded (159.5 and 160.9 eV) and unbonded free thiols (162.2 and 163.3 eV).<sup>[42]</sup> Finally, as expected for the ssDNA aptamer, the N atoms in the pyridinic groups and the pyrrole rings were assigned at 398.4, 399.5, and 401.1 eV—regarding N—C, N<sub>aromatic</sub>, and N—C—O contributions respectively,<sup>[43–45]</sup> while the P—O binding

energy from the phosphate groups were designated at 135.0 (2p<sub>3/2</sub>) and 136.7 eV (2p<sub>1/2</sub>).

All in all, the XPS results clearly demonstrated the successful synthesis of the ssDNA/Au@GeH heterostructure via surface engineering, whereas the results are well consistent with the TEM, UV-Vis spectroscopy, and FTIR characterization data.

## 2.2. Biorecognition Activity Using a Complementary Fluorescein-Labeled ssDNA Target

Having demonstrated the potential use of 2D-GeH as an unconventional substrate to harbour biorecognition agents (i.e., ssDNA aptamer), the next step was focused on elucidating its proper activity by optically monitoring a DNA hybridization process using a complementary ssDNA target labeled with fluorescein (FAM) at the 5'-end, named as FAM-DNA target. Figure 3a displays the excitation and emission spectra of the FAM-DNA target (control experiment), indicating a maximum emission at  $\lambda_{\text{Em}} = 520$  nm under excitation at  $\lambda_{\text{Ex}} = 497$  nm, in line with the literature.<sup>[46]</sup>

The optical experiment relies on incubating in a quartz cuvette a fixed amount of ssDNA/Au@GeH (0.1 mg mL<sup>-1</sup>) with different concentrations of the complementary FAM-DNA target at the nM range for 5 min in order to create a hybridization state-dependent optical signal. Figure 3b depicts the emission intensity signals of the FAM-DNA target at different concentrations (from 0 to 1.2 nM) in the presence of the ssDNA/Au@GeH heterostructure. Interestingly, the fluorescence of the FAM-DNA target was completely quenched until reaching a concentration of 0.80 nM. This quenching phenomenon can be explained through a photoinduced-electron-transfer (PET) effect due to the hybridization of the FAM-DNA target with the complementary



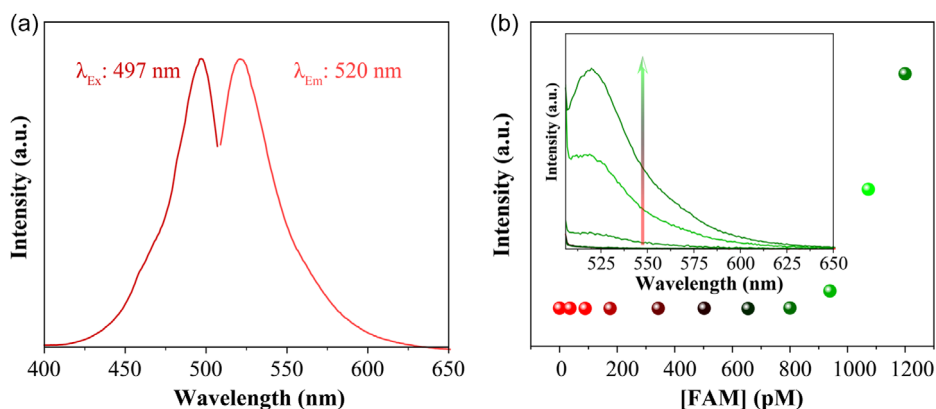


**Figure 3.** Optical evaluation of the ssDNA/Au@GeH biorecognition activity via DNA hybridization. a) The excitation and emission spectra of the FAM-DNA target. b) Emission intensity signals of the FAM-DNA target at different concentrations in the presence of the ssDNA/Au@GeH heterostructure. All measurements were recorded at room temperature.

nucleotide bases of the ssDNA/Au@GeH. It is known that this PET phenomenon clearly depends on the proximity of the fluorophore (FAM) with a guanine base from a complementary strand, where the quencher fluorophore acts as an electron acceptor in the excited state and the guanine base as an electron donor.<sup>[47]</sup> Upon 0.80 nM, the fluorescence signal rapidly increased due to the presence of a free FAM target in the medium, suggesting the complete consumption of active sites in the ssDNA/Au@GeH heterostructure. Consequently, the optical monitoring of the hybridization process not only revealed the proper activity of the biorecognition unit once it is immobilized onto the 2D-Xene, but also provided an accurate estimation of the number of active sites on the ssDNA/Au@GeH heterostructure, being quantified at 16 pmol of biorecognition unit per mg of sample.

### 2.3. Electrochemical Determination of Cocaine Drug via Cocaine-Binding Aptamer

The abuse of addictive drugs like cocaine is recognized as a worldwide challenge leading to both society and health problems, pointing out the critical significance of prompt detection toward drugs. In this regard, nanosystem-based biosensors provide a promising avenue for the specific determination of biomarkers at ultra-trace levels.<sup>[48,49]</sup> Considering the specificity of the ssDNA aptamer employed toward cocaine determination, the next step was focused on exploiting the ssDNA/Au@GeH heterostructure as an unconventional electrochemical biorecognition system. For this goal, 15  $\mu\text{L}$  of a 1  $\text{mg mL}^{-1}$  aqueous dispersion of ssDNA/Au@GeH was drop-casted onto a FTO surface and used as the working electrode. Remarkably, a home-made 3D-printed electrochemical cell was designed to operate with an embedded bottom working electrode (see Figure S3, Supporting Information for architecture schematization). Having a cell configuration based on a bottom working electrode allowed us to overcome the material leakage observed with the conventional top working electrode during operando.

Prior to electroanalytical application, the electrochemical characteristics of the ssDNA/Au@GeH heterostructure were evaluated by means of cyclic voltammetry (CV) and EIS, using the

forementioned home-made 3D-printed electrochemical cell filled with the conventional  $[\text{Fe}(\text{CN})_6]^{3-/4-}$  redox marker. For comparison, the same experiments were conducted with both pristine 2D-GeH and Au@GeH as control materials. As shown in the cyclic voltammograms depicted in Figure S4, Supporting Information, the different (bio)functionalization stages presented shifts in the anodic and cathodic peaks, which brought a change in peak-to-peak separation (see Table S2, Supporting Information for further information). Theoretically, variations in peak current and separation of peak potentials at different electrode surfaces correlate with different electron-transfer resistances. Comparing to pristine 2D-GeH, the inherent metallic nature of Au-NPs improved the electronic conductivity of the material. Then, a slight decrease in the electrochemical activity was observed once the biorecognition component was anchored via Au–S interactions. This can be explained since the accumulation of ssDNA aptamer increases the negative charge due to the phosphate backbone, hindering the electron transfer between the negatively charged  $[\text{Fe}(\text{CN})_6]^{3-/4-}$  redox marker and the electrode surface. This electrochemical behaviour is in line with the charge transfer resistance ( $R_{\text{CT}}$ ) values collected by EIS (Figure S5, Supporting Information), being 58.4, 20.1, and 29.1  $\Omega$  for pristine 2D-GeH, Au@GeH, and ssDNA/Au@GeH heterostructure, respectively. In brief,  $R_{\text{CT}}$ —a parameter that corresponds to the semicircle diameter in the high-frequency domain—controls the electron-transfer kinetics of the redox probe at the electrode–electrolyte interface. Accordingly, the electrochemical characterization data demonstrated optimum electrochemical features for the ssDNA/Au@GeH heterostructure, while the electrochemical changes observed by CV and EIS corroborated the satisfactory achievement of each (bio)functionalization stage.

Next, the following step was focused on testing the electroanalytical ability of the ssDNA/Au@GeH heterostructure toward biosensing implementation via cocaine-binding aptamer (Figure 4). Briefly, the ssDNA aptamer utilized here (discovered by Stojanovic and co-workers)<sup>[50]</sup> was demonstrated to be specific toward cocaine biorecognition, since other structurally related derivatives of cocaine cannot bind. The cocaine–aptamer binding mechanism (see Figure S6, Supporting Information, for

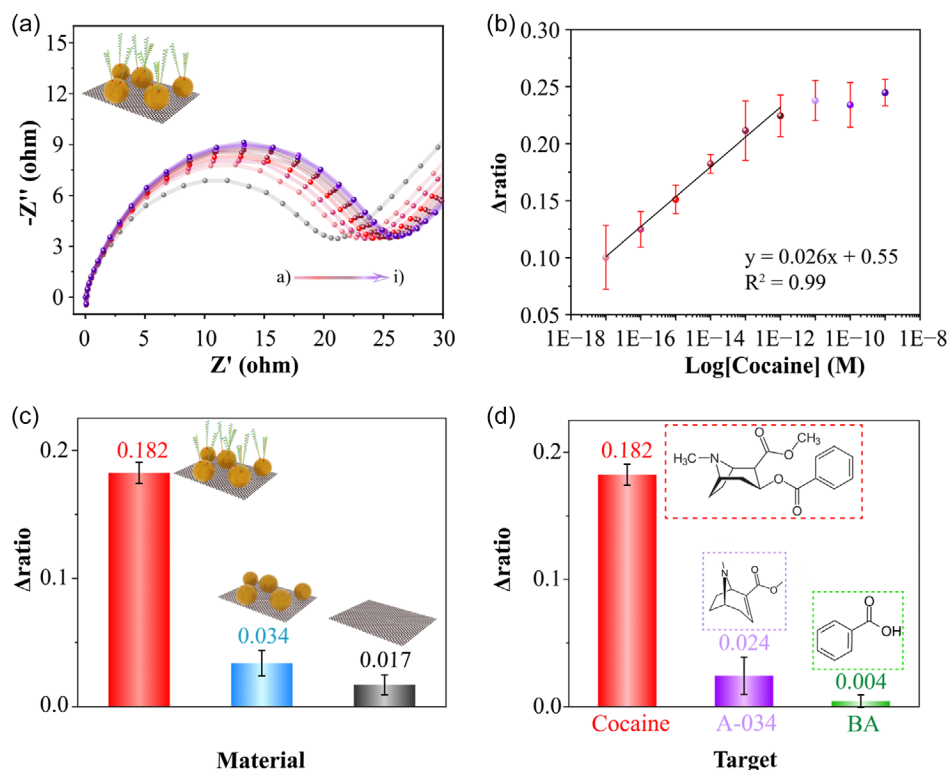


**Figure 4.** Electroanalytical performance of the ssDNA/Au@GeH electrochemical biosensor towards cocaine determination. a) EIS signals of electrochemical ssDNA/Au@GeH electrochemical biosensor before and after exposure to different concentrations of cocaine (a) 0, b)  $1 \times 10^{-17}$ , c)  $1 \times 10^{-16}$ , d)  $1 \times 10^{-15}$ , e)  $1 \times 10^{-14}$ , f)  $1 \times 10^{-13}$ , g)  $1 \times 10^{-12}$ , h)  $1 \times 10^{-11}$  and i)  $1 \times 10^{-10}$  M), and b) the resulting calibration curve. c)  $\Delta_{\text{ratio}}$  values extracted from EIS signals of the 2D-GeH, Au@GeH, and ssDNA/Au@GeH materials after exposure to  $1 \times 10^{-14}$  M cocaine, showing the specificity of the system. d)  $\Delta_{\text{ratio}}$  values extracted from EIS signals of the DNA/Au@GeH electrochemical biosensor towards  $1 \times 10^{-14}$  M of either cocaine, A-034, or BA, displaying the specificity of the system (inset: chemical structure of the targets). All the measurements were run per triplicate ( $n = 3$ ,  $\pm$ SD) using 10 mM  $[\text{Fe}(\text{CN})_6]^{3-/4-}$  in 0.1 M KCl as the electrolyte (incubation time: 5 min).

illustration) relies on the formation of a folded structure after cocaine interactions which consists of three stems (named as S1, S2, and S3) intersecting at a three-way junction, whose specificity is the consequence of its interaction with all faces of the cocaine molecule.<sup>[51]</sup>

The impedimetric assay relies on adding different aliquots of analyte (viz. cocaine drug) into the electrochemical cell filled with the electrolyte (i.e.,  $[\text{Fe}(\text{CN})_6]^{3-/4-}$ ) and aged for 5 min in order to promote the specific cocaine–aptamer supramolecular complex formation. The incubation time experiment revealed an optimum time of 5 min (Figure S7, Supporting Information). Then, the chemical inputs resulting from the cocaine–aptamer supramolecular complex formation were transduced into a readable electronic signal by means of  $R_{\text{CT}}$ . Figure 4a displays the EIS responses of the developed ssDNA/Au@GeH electrochemical biosensor toward different concentrations of cocaine drug, which are presented as Nyquist plots (real impedance,  $Z_{\text{real}}$  vs imaginary impedance,  $Z_{\text{imag}}$ ). An increase in the  $R_{\text{CT}}$  parameter with increasing the concentration of cocaine drug was observed, resulting in a wide working range from  $1 \times 10^{-17}$  to  $1 \times 10^{-12}$  M. This phenomenon can be ascribed to the steric hindrance of the insulating cocaine drug that blocks the electron-transfer rate constant of the redox marker. As shown in Figure 4b, the ssDNA/Au@GeH electrochemical biosensor

presented an excellent linear relationship with the logarithm of [cocaine], with a correlation coefficient of  $r^2 = 0.99$ . For the calibration curve construction, the acquired  $R_{\text{CT}}$  values were presented as  $\Delta_{\text{ratio}}$  [ $\Delta_{\text{ratio}} = (R_x - R_0)/R_0$ ] in order to obtain independent and reproducible results while comparing the different biosensors used here, where  $R_0$  and  $R_x$  are the  $R_{\text{CT}}$  values obtained before and after incubation with different [cocaine], respectively. The remarkable electroanalytical abilities of the ssDNA/Au@GeH electrochemical biosensor were confirmed by means of the outstanding detection limit yielded, being as low as  $4.9 \pm 0.1$  aM ( $n = 3$ ). This supposes that the developed 2D-GeH-based biorecognition system is capable of detecting ultra-trace levels of cocaine at a physiological buffered pH. Comparing to previously referenced electrochemical biosensors summarized in Table 1, the detection limit of the ssDNA/Au@GeH electrochemical biosensor was greatly improved by 6 decades of magnitude. Such an analytical enhancement must be attributed to a combination of two factors: i) the high surface-to-volume ratio nature of the 2D-GeH transducer rich in biorecognition components and ii) the strong sensitivity of EIS readouts, leading to a highly sensitive ssDNA/Au@GeH electrochemical biosensor capable of measuring traces of analyte.

Lastly, the specificity and selectivity of the devised electrochemical biosensor were explored using the mid-point

**Table 1.** Comparison of the electrochemical performance over 2D material-based biosensors to analyze cocaine.

Material	Linear range [M]	LOD	References
2D AuNCs@521-MOF	$1 \times 10^{-9}$ – $1 \times 10^{-6}$	$1.29 \times 10^{-12}$	[56]
MWCNTs/graphite	$2 \times 10^{-6}$ – $1.2 \times 10^{-3}$	$9.1 \times 10^{-7}$	[57]
Graphene/AuNPs	$1 \times 10^{-9}$ – $5 \times 10^{-7}$	$1 \times 10^{-9}$	[58]
3D-printed G-PLA	$2 \times 10^{-5}$ – $1 \times 10^{-4}$	$6 \times 10^{-6}$	[59]
Graphite SPE	$1 \times 10^{-4}$ – $5 \times 10^{-4}$	–	[60]
MnO <sub>2</sub> nanosheets	$1 \times 10^{-10}$ – $2 \times 10^{-8}$	$3.2 \times 10^{-11}$	[61]
MWCNTs	$1 \times 10^{-2}$ – $1.55 \times 10^{-1}$	–	[62]
ERGO	$1 \times 10^{-4}$ – $8 \times 10^{-4}$	$1.9 \times 10^{-8}$	[63]
EGO	$5 \times 10^{-8}$ – $1 \times 10^{-4}$	$5 \times 10^{-9}$	[64]
Graphene/graphite	$10 \times 10^{-6}$ – $70 \times 10^{-6}$	$2.4 \times 10^{-8}$	[65]
Multiplex laser-scribed graphene	$1 \times 10^{-11}$ – $1 \times 10^{-9}$	$9 \times 10^{-11}$	[66]
ssDNA/Au@GeH	$1 \times 10^{-17}$ – $1 \times 10^{-12}$	$4.9 \times 10^{-18}$	This work

concentration found in the linear working range ( $1 \times 10^{-14}$  M). On the one hand, the electroanalytical ability of both pristine 2D-GeH and Au@GeH toward the determination of the cocaine drug was interrogated (control experiments). As shown in Figure S8, Supporting Information, no significant  $R_{CT}$  changes were observed when using the control materials. Thus, while ssDNA/Au@GeH yielded a  $\Delta_{ratio}$  of 0.182, values as low as 0.017 and 0.034 were achieved by pristine 2D-GeH and Au@GeH, respectively (see Figure 4c). On the other hand, the selectivity of the ssDNA/Au@GeH was explored against two non-specific targets with cocaine-like chemical structures, such as anhydroecgonine methyl ester (A-034) and benzoic acid (BA). As shown in Figure S9, Supporting Information, no EIS changes were noticed after exposing the electrochemical biosensor to a fixed concentration of non-specific targets, indicating that the interfering signals were around 10% (see Figure 4d for electroanalytical  $\Delta_{ratio}$  values). All in all, these anti-interfering results demonstrate: i) that no unspecific adsorption occurs without the presence of the specific biorecognition unit and ii) the key role of the biorecognition unit (i.e., ssDNA aptamer) for selectively interacting with the target via cocaine–aptamer complex formation.

### 3. Conclusions

In summary, a straightforward biofunctionalization approach has been devised to robustly integrate biorecognition components onto commercially available 2D-GeH for the development of highly sensitive biosensing systems. The method relies on the immobilization of Au-NPs onto pristine 2D-GeH via the OM approach, followed by the anchoring of thiolated biorecognition agents through Au–S bond interactions, using an ssDNA aptamer as a model ligand. The morphology, chemical bonding, and elemental states of the resulting ssDNA/Au@GeH heterostructure were systematically characterized, demonstrating: i) the suitability of 2D-GeH as an unconventional support to stabilize Au-NPs, as well as ii) the successful assembly of the ssDNA aptamer onto Au@GeH via Au–S bond formation. As a

proof-of-principle, the impedimetric determination of cocaine drug was considered by taking advantage of the specific cocaine–aptamer binding that promotes electronic changes by means of  $R_{CT}$ . From the electroanalytical perspective, the biosensor was capable of detecting cocaine at attomolar levels in physiological pH, while presenting selectivity and specificity. To the best of our knowledge, this is the lowest detection limit for cocaine found in literature by far. This is a very appealing result since it allows a high degree of sample dilution that might help to avoid any undesired interfering target. Consequently, our findings pave the bases toward the custom design and implementation of a new family of highly sensitive nanoarchitectonics by interfacing DNA aptamers with 2D-GeH, providing a valuable platform for the development of point-of-care devices with electronic readouts. Finally, the chemical biofunctionalization strategy is general and might be simply extended by tailoring the biorecognition agent.

### 4. Experimental Section

**Chemicals and Reagents:** 2D-GeH, cocaine, and anti-interfering analytes (anhydroecgonine methyl ester, A-034 and benzoic acid, BA) were purchased from Sigma-Aldrich (St. Louis, MO, USA). The ssDNA aptamer for cocaine containing a thiol substituent attached to a six-carbon linker at the 3' end (5'-TGA-GGG-GGA-GAC-AAG-GAA-AAT-CCT-TCA-ATG-AAG-TGG-GTC-TCC-CTT-TTT-TTT-SS(CH<sub>2</sub>)<sub>6</sub>-3') and the complementary FAM-labeled short ssDNA target (5'-GTC-TCC-CCC-TCA-GA-TAG-CTT-ATC-AGA-CTG-ATG-TTG-ACC-6FAM-3') were selected from literature—the complementary portions have been boldfaced<sup>[52]</sup>—and were also supplied and purified through high performance liquid chromatography (HPLC) by Sigma-Aldrich. The disulfide bond of the purchased ssDNA aptamer was reduced to its active sulfhydryl form by following the conventional protocol.<sup>[53]</sup> Chloro(tetrahydrothiophene)gold(I) ([Au(tht)Cl]) was furnished by Strem Chemicals, Inc. (Boston, MA, USA). Hydrogen (H<sub>2</sub>) gas was purchased from Air Liquide (Alphagaz). Other chemical reagents were of the highest grade available and used as received.

**Apparatus and Procedures:** The morphology of pristine 2D-GeH, Au@GeH, and DNA/Au@GeH was studied by transmission electron microscopy (TEM), using a JEM-2011 unit with an acceleration voltage of 200 kV. The elemental statuses were studied by X-ray photoelectron spectroscopy (XPS), using a Phoibos 150 analyzer (SPECS GmbH, Berlin,

Germany) in ultrahigh vacuum conditions (base pressure  $5 \times 10^{-10}$  mbar) with a monochromatic aluminum  $K_{\alpha}$  X-ray source (1486.74 eV). Fluorometric measurements were run using a Cary Eclipse Fluorimeter. Electrochemical experiments were conducted in a home-made 3D-printed cell (see Figure S3, Supporting Information) using a PalmSens4 potentiostat/galvanostat equipped with PSTrace software. Measurements were run using an Ag/AgCl (sat. KCl) electrode, a Pt wire electrode, and a fluorine-doped tin oxide glass (FTO) electrode as reference, counter, and working electrodes, respectively.

**Fluorescence Measurements:** The fluorescence measurements were carried out in a quartz cuvette filled with a fixed concentration of ssDNA/Au@GeH heterostructure. Along the measurements, different aliquots of FAM-DNA target were dropped into the cuvette and aged for 5 min to induce the DNA hybridization process. Afterwards, the emission intensity signals were recorded at  $\lambda_{em} = 520$  nm, using an excitation wavelength of  $\lambda_{ex} = 497$  nm.

**Fabrication of ssDNA/Au@GeH Electrochemical Biosensor:** The bare FTO (transducer support) was first washed by Milli Q water, acetone, and ethanol. Then, 15  $\mu$ L of a 1 mg mL<sup>-1</sup> dispersion of ssDNA/Au@GeH in THF was drop-casted onto the cleaned FTO, resulting in the electrochemical biosensor. The same approach was carried out to prepare the control electrodes with both pristine 2D-GeH and Au@GeH.

**Electrochemical Measurements:** The electrochemical characterization was carried out by means of cyclic voltammetry (CV) and EIS, using a 10 mM [Fe(CN)<sub>6</sub>]<sup>3-/4-</sup> buffered solution (pH 7.2) as a benchmark redox marker. The electroactive area (A) was calculated following the modified Randles–Ševčík equation (Equation (1)),<sup>[15]</sup> while the heterogeneous electron-transfer (HET) constant was calculated according to the Nicholson equation (Equation (2)).<sup>[54]</sup>

$$I_p = 3.01 \times 10^5 \cdot (\alpha D_{red} \nu)^{1/2} \cdot A \cdot C_{red}^* \quad (1)$$

$$k_0 = \Psi(\pi D_0 n F \nu / RT)^{1/2} \quad (2)$$

where  $I_p$  was current peak collected from CV curves,  $\Psi$  has a linear correlation with the inverse logarithm value of  $\Delta E$ , in this system  $\Psi = \exp(-0.00423 \times \Delta E - 0.09)$ ,  $C_{red} = 10^{-5}$  mol mL<sup>-1</sup>,  $\nu = 50$  mV s<sup>-1</sup>,  $D_{red}$  was the diffusion coefficient of reacting species,  $D_{red} \approx D_0 = 0.762 \times 10^{-5}$  cm<sup>2</sup> s<sup>-1</sup>, and  $RT/F = 25.7$  mV at 25 °C (ambient condition).

The electroanalytical assay was carried out by exposing the ssDNA/Au@GeH electrochemical biosensor to different [cocaine] (incubation time: 5 min). EIS signals were collected by means of charge transfer resistance ( $R_{CT}$ ) values. All measurements were run per triplicate ( $n = 3$ ). A normalization procedure in terms of  $\Delta_{ratio}$  was necessary to properly compare the three independent electrodes used. The limit of detection (LOD) was calculated from the standard formula  $LOD = 3s_{blank}/S$ ,<sup>[55]</sup> where  $s_{blank}$  is the standard deviation from the signal obtained from the blank,  $S$  is the slope of the calibration curve, and the number 3 comes from the required 90% level confidence.

## Supporting Information

Supporting Information is available from the Wiley Online Library or from the author.

## Acknowledgements

Y.L. acknowledges the program of China Scholarships Council (grant no. 202206250016). Y.L. is enrolled in the UAB Chemistry PhD program. X.S. thanks ICREA for the ICREA Academia Prize 2020. X.S. and J.G.-A. thank MINECO/FEDER (PID2019-104171RB-I00) and MICINN (PID2023-146787OB-I00) for financial support. J.M. is indebted to the Ramón y Cajal Program (RYC2021-033820-I Fellowship) funded by MCIN/AEI/10.13039/501100011033 and by the European Union “NextGenerationEU/PRTR”.

## Conflict of Interest

The authors declare no conflict of interest.

## Author Contributions

**Yiming Lei** and **Ángel Campos-Lendínez:** Investigation, Formal analysis, Validation, Writing—review & editing. **Jordi García-Antón** and **Xavier Sala:** Supervision, Funding acquisition, Writing—review & editing. **Jose Muñoz:** Conceptualization, Validation, Supervision, Writing—original draft, Writing—review & editing, Funding acquisition.

## Data Availability Statement

The data that support the findings of this study are available from the corresponding author upon reasonable request.

## Keywords

2D materials, aptasensor, DNA, electrochemical sensor, germanene

Received: May 15, 2024

Revised: August 8, 2024

Published online:

- [1] J. Xie, N. M. Patoary, G. Zhou, M. Y. Sayyad, S. Tongay, I. S. Esqueda, *Nanotechnology* **2022**, *33*, 225702.
- [2] T. Huang, J. Ding, Z. Liu, R. Zhang, B. Zhang, K. Xiong, L. Zhang, C. Wang, S. Shen, C. Li, P. Yang, F. Qiu, *eScience* **2022**, *2*, 319.
- [3] Z.-Y. Yan, Z. Hou, F. Wu, R. Zhao, J. Yan, A. Yan, Z. Wang, K.-H. Xue, H. Liu, H. Tian, Y. Yang, T.-L. Ren, *2D Mater.* **2023**, *10*, 045026.
- [4] W. Fei, J. Trommer, M. C. Lemme, T. Mikolajick, A. Heinz, *InfoMat* **2022**, *4*, e12355.
- [5] Q. Zou, J. Qiu, Y. Zang, H. Tian, L. Venkataraman, *eScience* **2023**, *3*, 100115.
- [6] D. Xu, J. Li, Y. Xiong, H. Li, J. Yang, W. Liu, L. Jiang, K. Qu, T. Zhao, X. Shi, S. Zhang, D. Shan, X. Chen, H. Zeng, *InfoMat* **2023**, *5*, e12398.
- [7] A. F. Carvalho, B. Kulyk, A. J. S. Fernandes, E. Fortunato, F. M. Costa, *Adv. Mater.* **2022**, *34*, 2101326.
- [8] A. G. Olabi, M. A. Abdelkareem, T. Wilberforce, E. T. Sayed, *Renewable Sustainable Energy Rev.* **2021**, *135*, 110026.
- [9] H. Huang, H. Shi, P. Das, J. Qin, Y. Li, X. Wang, F. Su, P. Wen, S. Li, P. Lu, F. Liu, Y. Li, Y. Zhang, Y. Wang, Z. Wu, H. Cheng, *Adv. Funct. Mater.* **2020**, *30*, 1909035.
- [10] J. Muñoz, J. Oliver-De La Cruz, G. Forte, M. Pumera, *Biosens. Bioelectron.* **2023**, *226*, 115113.
- [11] Z. Xie, B. Zhang, Y. Ge, Y. Zhu, G. Nie, Y. Song, C.-K. Lim, H. Zhang, P. N. Prasad, *Chem. Rev.* **2022**, *122*, 1127.
- [12] J. Muñoz, *Adv. Mater.* **2024**, *36*, 2305546.
- [13] S. Ng, M. Pumera, *Adv. Mater.* **2023**, *35*, 2207196.
- [14] J. Muñoz, M. Palacios-Corella, I. J. Gómez, L. Zajíčková, M. Pumera, *Adv. Mater.* **2022**, *34*, 2206382.
- [15] N. F. Rosli, N. Rohaizad, J. Sturala, A. C. Fisher, R. D. Webster, M. Pumera, *Adv. Funct. Mater.* **2020**, *30*, 1910186.
- [16] M. Palacios-Corella, J. Muñoz, M. Pumera, *Nanoscale* **2022**, *14*, 18167.
- [17] P. K. Roy, T. Hartman, J. Šturala, J. Luxa, M. Melle-Franco, Z. Sofer, *ACS Appl. Mater. Interfaces* **2023**, *15*, 25693.
- [18] U. Srimathi, V. Nagarajan, R. Chandiramouli, *Comput. Theor. Chem.* **2018**, *1130*, 68.



- [19] U. Srimathi, V. Nagarajan, R. Chandiramouli, *Appl. Surf. Sci.* **2019**, 475, 990.
- [20] H. L. Chia, J. Sturla, R. D. Webster, M. Pumera, *Adv. Funct. Mater.* **2021**, 31, 2011125.
- [21] R. R. Xia Lim, J. Sturla, V. Mazanek, Z. Sofer, A. Bonanni, *Talanta* **2024**, 270, 125509.
- [22] Z. Song, W. L. Ang, J. Sturla, V. Mazanek, P. Marvan, Z. Sofer, A. Ambrosi, C. Ding, X. Luo, A. Bonanni, *ACS Appl. Nano Mater.* **2021**, 4, 5164.
- [23] M. Tasbihi, F. Fresno, I. Álvarez-Prada, A. Acharjya, A. Thomas, L. Escriche, N. Romero, X. Sala, V. A. de la Peña O'Shea, J. García-Antón, *J. CO<sub>2</sub> Util.* **2021**, 50, 101574.
- [24] B. R. Baker, R. Y. Lai, M. S. Wood, E. H. Doctor, A. J. Heeger, K. W. Plaxco, *J. Am. Chem. Soc.* **2006**, 128, 3138.
- [25] L. Gao, H. Wang, Z. Deng, W. Xiang, H. Shi, B. Xie, H. Shi, *New J. Chem.* **2020**, 44, 2571.
- [26] A. Mokhtarzadeh, J. Ezzati Nazhad Dolatabadi, K. Abnous, M. de la Guardia, M. Ramezani, *Biosens. Bioelectron.* **2015**, 68, 95.
- [27] S. Bilge, B. Dogan-Topal, M. M. Gürbüz, A. Yücel, A. Sinağ, S. A. Ozkan, *TrAC Trends Anal. Chem.* **2022**, 157, 116768.
- [28] J. Muñoz, R. Montes, M. Baeza, *TrAC Trends Anal. Chem.* **2017**, 97, 201.
- [29] I. Álvarez-Prada, D. Peral, M. Song, J. Muñoz, N. Romero, L. Escriche, A. Acharjya, A. Thomas, R. Schomäcker, M. Schwarze, X. Sala, M. Tasbihi, J. García-Antón, *Renewable Energy* **2021**, 168, 668.
- [30] T. Giousis, G. Potsi, A. Kouloumpis, K. Spyrou, Y. Georgantas, N. Chalmpes, K. Dimos, M. Antoniou, G. Papavassiliou, A. B. Bourlinos, H. J. Kim, V. K. S. Wadi, S. Alhassan, M. Ahmadi, B. J. Kooi, G. Blake, D. M. Balazs, M. A. Loi, D. Gournis, P. Rudolf, *Angew. Chem. Int. Ed.* **2021**, 60, 360.
- [31] Z. Liu, Z. Lou, Z. Li, G. Wang, Z. Wang, Y. Liu, B. Huang, S. Xia, X. Qin, X. Zhang, Y. Dai, *Chem. Commun.* **2014**, 50, 11046.
- [32] A. Zuber, M. Purdey, E. Schartner, C. Forbes, B. van der Hoek, D. Giles, A. Abell, T. Monro, H. Ebendorff-Heidepriem, *Sens. Actuators, B* **2016**, 227, 117.
- [33] J. C. Sutherland, K. P. Griffin, *Radiat. Res.* **1981**, 86, 399.
- [34] E. Bianco, S. Butler, S. Jiang, O. D. Restrepo, W. Windl, J. E. Goldberger, *ACS Nano* **2013**, 7, 4414.
- [35] E. Leonova, K. Shvirksts, V. Borisovs, E. Smelovs, J. Sokolovska, E. Bisenieks, G. Duburs, M. Grube, N. Sjakste, *PeerJ* **2020**, 8, e10061.
- [36] S. Liang, L. Wu, H. Liu, J. Li, M. Chen, M. Zhang, *Biosens. Bioelectron.* **2019**, 126, 30.
- [37] C. Su, Z. Yin, Q.-B. Yan, Z. Wang, H. Lin, L. Sun, W. Xu, T. Yamada, X. Ji, N. Zettsu, K. Teshima, J. H. Warner, M. Dincă, J. Hu, M. Dong, G. Su, J. Kong, J. Li, *Proc. Natl. Acad. Sci.* **2019**, 116, 20844.
- [38] Y. Feng, G. Wang, Y. Chang, Y. Cheng, B. Sun, L. Wang, C. Chen, H. Zhang, *Nano Lett.* **2019**, 19, 4478.
- [39] F. Vitale, I. Fratoddi, C. Battocchio, E. Piscopiello, L. Tapfer, M. V. Russo, G. Polzonetti, C. Giannini, *Nanoscale Res. Lett.* **2011**, 6, 103.
- [40] Z. Tang, B. Xu, B. Wu, M. W. Germann, G. Wang, *J. Am. Chem. Soc.* **2010**, 132, 3367.
- [41] F. Wang, R. J. Wong, J. H. Ho, Y. Jiang, R. Amal, *ACS Appl. Mater. Interfaces* **2017**, 9, 30575.
- [42] J. Jia, A. Kara, L. Pasquali, A. Bendounan, F. Sirotti, V. A. Esaulov, *J. Chem. Phys.* **2015**, 143, 104702.
- [43] A. Singh, R. Meena, *Polym. Bull.* **2023**, 80, 6835.
- [44] I. G. Subramani, V. Perumal, S. C. B. Gopinath, N. M. Mohamed, N. Joshi, M. Ovinis, L. L. Sze, *J. Taiwan Inst. Chem. Eng.* **2020**, 116, 26.
- [45] M. Yahaya, *IOP Conf. Ser. Mater. Sci. Eng.* **2020**, 805, 012007.
- [46] Jyoti, J. Muñoz, M. Pumera, *ACS Appl. Mater. Interfaces* **2023**, 15, 58548.
- [47] M. Torimura, S. Kurata, K. Yamada, T. Yokomaku, Y. Kamagata, T. Kanagawa, R. Kurane, *Anal. Sci.* **2001**, 17, 155.
- [48] M. Fukuyama, *Bull. Chem. Soc. Jpn.* **2023**, 96, 1252.
- [49] S. K. Patel, J. Wekalao, H. B. Albargi, M. Jalalah, A. H. M. Almwagani, A. Armghan, *Plasmonics* **2024**, <https://doi.org/10.1007/s11468-024-02224-5>.
- [50] M. N. Stojanovic, P. de Prada, D. W. Landry, *J. Am. Chem. Soc.* **2000**, 122, 11547.
- [51] A. Sachan, M. Ilgu, A. Kempema, G. A. Kraus, M. Nilsen-Hamilton, *Anal. Chem.* **2016**, 88, 7715.
- [52] C. Ma, W. Wang, Q. Yang, C. Shi, L. Cao, *Biosens. Bioelectron.* **2011**, 26, 3309.
- [53] A. Van Aerschot, J. Rozenski, *J. Am. Soc. Mass Spectrom.* **2006**, 17, 1397.
- [54] R. S. Nicholson, *Anal. Chem.* **1965**, 37, 1351.
- [55] Analytical Chemistry Division, *Spectrochim. Acta, Part B* **1978**, 33, 241.
- [56] F. Su, S. Zhang, H. Ji, H. Zhao, J.-Y. Tian, C.-S. Liu, Z. Zhang, S. Fang, X. Zhu, M. Du, *ACS Sens.* **2017**, 2, 998.
- [57] X. Li, Z. Chen, Y. Zhong, F. Yang, J. Pan, Y. Liang, *Anal. Chim. Acta* **2012**, 710, 118.
- [58] B. Jiang, M. Wang, Y. Chen, J. Xie, Y. Xiang, *Biosens. Bioelectron.* **2012**, 32, 305.
- [59] R. G. Rocha, J. S. Ribeiro, M. H. P. Santana, E. M. Richter, R. A. A. Muñoz, *Anal. Methods* **2021**, 13, 1788.
- [60] A. Florea, T. Cowen, S. Piletsky, K. De Wael, *Talanta* **2018**, 186, 362.
- [61] Z. Chen, M. Lu, *Talanta* **2016**, 160, 444.
- [62] L. Asturias-Arribas, M. A. Alonso-Lomillo, O. Domínguez-Renedo, M. J. Arcos-Martínez, *Anal. Chim. Acta* **2014**, 834, 30.
- [63] D. P. Rocha, R. M. Dornellas, E. Nossol, E. M. Richter, S. G. Silva, M. H. P. Santana, R. A. A. Munoz, *Electroanalysis* **2017**, 29, 2418.
- [64] Y. Lei, B. D. Osseonon, P.-L. Trahan, J. Chen, J. Perreault, A. C. Tavares, *ACS Appl. Mater. Interfaces* **2023**, 15, 35580.
- [65] A. García-Miranda Ferrari, H. M. Elbardisy, V. Silva, T. S. Belal, W. Talaat, H. G. Daabees, C. E. Banks, D. A. C. Brownson, *Anal. Methods* **2020**, 12, 2133.
- [66] D. Beduk, T. Beduk, J. I. de Oliveira Filho, A. Ait Lahcen, E. Aldemir, E. Guler Celik, K. N. Salama, S. Timur, *ACS Appl. Mater. Interfaces* **2023**, 15, 37247.